

Theoretical investigation of a miniature microwave driven plasma jet

Michael Klute^{1,4} , Horia-Eugen Porteanu² , Ilija Stefanovic³ , Wolfgang Heinrich², Peter Awakowicz³ and Ralf Peter Brinkmann¹ 

¹ Theoretical Electrical Engineering, Ruhr University Bochum, Germany

² Microwave Department, Ferdinand-Braun-Institut, Berlin, Germany

³ Electrical Engineering and Plasma Technology, Ruhr University Bochum, Germany

E-mail: Michael.Klute@ruhr-uni-bochum.de

Received 31 January 2020, revised 28 April 2020

Accepted for publication 19 May 2020

Published 29 June 2020



Abstract

Radio frequency driven plasma jets are compact plasma sources which are used in many advanced fields such as surface engineering or biomedicine. The MMWICP (miniature microwave ICP) is a particular variant of that device class. Unlike other plasma jets which employ capacitive coupling, the MMWICP uses the induction principle. The jet is integrated into a miniature cavity structure which realizes an LC-resonator with a high quality factor. When excited at its resonance frequency, the resonator develops a high internal current which—transferred to the plasma via induction—provides an efficient source of RF power. This work presents a theoretical model of the MMWICP. The possible operation points of the device are analyzed. Two different regimes can be identified, the capacitive *E*-mode with a plasma density of $n_e \approx 5 \times 10^{17} \text{m}^{-3}$, and the inductive *H*-mode with densities of $n_e \geq 10^{19} \text{m}^{-3}$. The *E* to *H* transition shows a pronounced hysteresis behavior.

Keywords: plasma jet, inductively, microwave, miniature, ICP, RF

(Some figures may appear in colour only in the online journal)

1. Introduction

Plasma processes can be classified into ‘direct’ and ‘remote’ [1]. In direct plasma processes, the generation and application of the plasma are co-located: a work-piece is introduced into a plasma chamber and processed therein. In remote plasma processes, plasma generation and plasma application are spatially separated. In the source, the plasma is only generated; it emerges from there as a stream of energetic particles that strikes the object to be treated. Remote plasma processes have significant advantages: the sources are relatively economic, quite small, and can be handled very flexibly. They can be employed in a wide pressure range: low pressure (about 10–10³Pa) is of interest, e.g., for plasma enhanced thin film

deposition; atmospheric pressure (10⁵Pa) allows medical and environmental applications.

Among the sources suitable for remote plasma processes, radio frequency driven (RF) plasma jets play a particularly important role [2–6]. They are usually operated in a capacitive mode: the RF power is applied to a set of co-planar or co-axial electrodes which results in a strong electric field in the interior of the jet. If the field strength exceeds the gas breakdown value, the avalanche effects sets in and the discharge ignites. The emerging plasma organizes itself into a quasi-neutral bulk and strongly electron depleted boundary sheaths.

Capacitive coupling enables plasma jets with a simple structure and robust ignition behavior. However, the operation principle has one serious disadvantage: the RF power is fed through the boundary sheaths which are hence modulated, become wider, and, acting as ‘rectifiers’, develop a higher voltage drop. This voltage, in turn, accelerates the positive ions which then strike the electrodes with high kinetic energy. As the power increases, more and more energy is channeled into

⁴ Author to whom any correspondence should be addressed.



Original content from this work may be used under the terms of the [Creative Commons Attribution 4.0 licence](https://creativecommons.org/licenses/by/4.0/). Any further distribution of this work must maintain attribution to the author(s) and the title of the work, journal citation and DOI.

the ion component. This limits the achievable plasma density and causes strong erosion and heating of the electrodes, even the ignition of parasitic arcs.

An alternative to capacitive coupling is inductive coupling [7]. A coil situated outside of the plasma chamber is driven by the RF power and creates a time varying magnetic field. This magnetic field induces an electric field, which then drives a strong current in the plasma. Provided the configuration is sufficiently symmetrical, the current is parallel to the sheaths; modulation and increased sheath voltage are avoided. A larger fraction of the supplied RF power is channeled into the electron component, which leads to a higher plasma density, and a smaller fraction into the ion component, which reduces electrode erosion and heating. Inductively coupled plasmas (ICPs) have found use in many different areas [8–12].

Attempts have been made to realize the principle of inductive coupling also for plasma jets. An early example is the induction-coupled plasma torch [13]. This was, however, a relatively large device which generated a plasma in thermal equilibrium. Research on small scale ICP jets was less successful [14–16]: it was not clear whether the inductive ‘*H*-mode’ was reached or just a parasitic ‘*E*-mode’ caused by the capacitive coupling of the RF voltage at the coil. The underlying problem can be understood in terms of the following scaling law (after [7]) which clearly favors sources of large size. For an ICP with chamber height $H \approx$ radius R , the absorbed power P_{abs} is a function of the coil winding number N , the driving current I , the plasma conductivity σ_{eff} , and the skinddepth λ_s :

$$P_{\text{abs}} = \begin{cases} N^2 I^2 R^3 / \sigma_{\text{eff}} \lambda_s^4 & \text{for } \lambda_s \gtrsim R \\ N^2 I^2 / \sigma_{\text{eff}} \lambda_s & \text{for } \lambda_s \lesssim R. \end{cases} \quad (1)$$

It is apparent that ICPs can only be operated efficiently if the skinddepth is smaller than the chamber dimension R , or at least comparable. Since λ_s scales with the electron density $n_e^{-1/2}$, this requires a high level of absorbed power P_{abs} . The conductivity σ_{eff} is not independent but a function of the gas composition, the pressure, the temperature, and the electron density. Increasing the coil winding number N is not helpful; it increases the inductance of the coil, amplifies the RF voltage drop, and favors the parasitic *E*-mode. The only available option is to provide a sufficiently high coil current I . This is not an easy task: because of the low equivalent plasma impedance, the required values are immense.

Porteanu *et al* found a solution [17]: their novel MMWICP (miniature microwave ICP) integrates the jet into a structure that acts as an LC resonator with a high quality factor Q . When excited at its resonance, the circuit effectively realizes an impedance transformation; the coils carry an RF current that is much higher than the driving current from the source. Reference [17] and two follow-up studies [18, 19] demonstrated the feasibility of the concept and showed that the *H*-mode with high plasma density can indeed be achieved.

The purpose of this research is to define and analyze a mathematical model of the MMWICP. Section 2 will provide a detailed description of the prototype which is shown in figures 1 and 2. Section 3 gives an analytical model of the electromagnetic field and the power absorption; section 4 pro-

vides a global plasma model. Section 5 couples these models self-consistently for argon at a pressure of $p = 100\text{Pa}$ and a gas temperature of $T_g = 800\text{K}$ and studies the operation principles of the MMWICP. The paper ends with a summary and discussion.

2. The demonstrator and its idealization

A visualization of the jet demonstrator is shown in figure 1; figure 2 depicts its cross section. The device is based on a block of copper with a width of $W = 34\text{ mm}$, a height of $H = 10\text{ mm}$, and a depth of $L = 8\text{ mm}$ [17]. It realizes a double jet with two parallel plasma discharges and two separate plasma effluents. Two parallel boreholes of $R = 3.5\text{ mm}$ radius form cavities which are connected by a milled planar slit of $L_s = 11\text{ mm}$ length and $d_s = 0.22\text{ mm}$ width. Two dielectric tubes with a wall thickness of $d = 1\text{ mm}$ are passed through the parallel cavities to conduct the process gas and to house the plasma. The MMWICP is encapsulated and shielded by a solid 8 mm thick aluminum housing.

Electrically, the structure can be interpreted as a lumped-element LC-resonator with a vacuum resonance frequency of $f_{\text{res}} = 2.3\text{GHz}$: the cavities act like coils with a winding number of one, the slit behaves as a capacitor. A lumped-element interpretation is possible because the resonance frequency is well below the frequency of any genuine cavity mode: all relevant dimensions are much smaller than a quarter wavelength $\lambda_{\text{res}}/4 = 33\text{ mm}$.

This study is conducted under the assumption of translational invariance in the z direction; the resonator is interpreted as an $L = 8\text{ mm}$ thick slice of a formally infinitely long device. This simplifies the analysis considerably. For example, the inductance of the cavities can be calculated as $L_c = \mu_0 \pi R^2 / L = 6\text{ nH}$, the capacitance of the slit as $C_s = \epsilon_0 L L_s / d_s = 3.5\text{ pF}$. The resonance frequency is then $f_{\text{res}} = 1/2\pi \sqrt{L_c C_s / 2} = 1.5\text{ GHz}$. The deviation from the experimental value can be seen as a measure of the modeling error.

The jet is fed by a power supply of $Z_0 = 50\Omega$ impedance. A matching network (see figure 3) is realized by two inductive elements. The $L_L = 8\text{ mm}$ long and $2R_L = 0.8\text{ mm}$ thick conductor that runs in a bore of $2R_B = 5\text{ mm}$ to the slit corresponds to an inductance of $L_{\text{ser}} \approx 3\text{ nH}$. The second inductance of $L_{\text{par}} \approx 0.7\text{ nH}$ is realized by a strip conductor connected to ground. Altogether, the following admittance and impedance result, where the admittance $Y_p(n_e, \omega)$ of a single plasma-filled cavity will be derived in the next chapter. The admittance of the combined system of plasma, resonator and matching network follows from the lumped element description and is given by:

$$Y_s(\omega, n_e) = \frac{1}{Z_s(\omega, n_e)} = \frac{1}{(2Y_p(n_e, \omega) + i\omega C_{\text{res}})^{-1} + i\omega L_{\text{ser}}} + \frac{1}{i\omega L_{\text{par}}}. \quad (2)$$

The complex reflection coefficient is then

$$\Gamma = \frac{Z_s - Z_0}{Z_s + Z_0} = \frac{1 - Z_0 Y_s}{1 + Z_0 Y_s}. \quad (3)$$

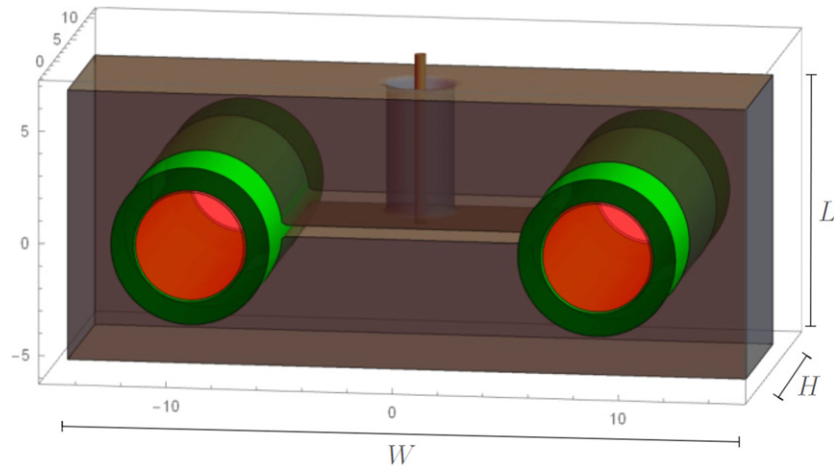


Figure 1. Visualization of the MMWICP plasma jet. Brown represents the resonator made of copper, green the dielectric tube of quartz, and red the plasma itself.

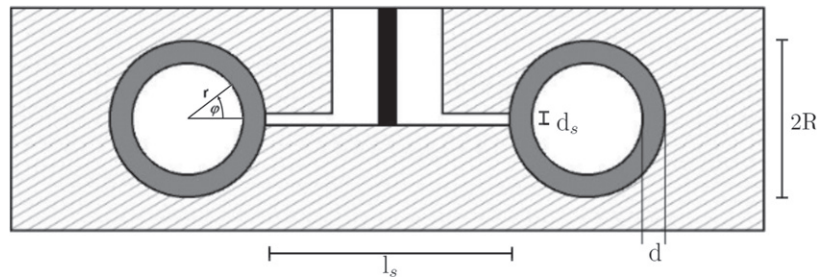


Figure 2. Cross section and inner dimensions of the resonator, where R represents the radius of the two parallel boreholes, d the wall thickness of the dielectric tubes, L_s the length, and d_s the width of the planar slit. The coordinate system used for calculation is shown on the left.

3. Electromagnetic model of a single jet

For an electromagnetic model of the cavity interior, a system of cylindrical coordinates (r, ϕ, z) in natural orientation is erected (see figure 2). A concentric three-zone structure is assumed: the inner zone from $r = 0$ to $r = R - d - \delta$ contains plasma of a constant electron density n_e and carries the zone index p , the zone from $r = R - d - \delta$ to $r = R - d$ is the electron-depleted sheath (index s), and the zone from $r = R - d$ to $r = R$ denotes the dielectric tube (index d). The structure is static; the microwave modulation of the sheath was verified to be negligible. The magnetic field \mathbf{B} and the electric field \mathbf{E} are assumed to be invariant in the z -direction.

However, because of the capacitor gap at $\phi = 0$, there is no azimuthal symmetry and the fields depend on both r and ϕ . In a time-harmonic approach, they are written as follows, where $n \in \{p, s, d\}$ refers to the zones defined above:

$$\mathbf{B}^{(n)}(r, \phi, t) = \text{Re} \left(\underline{B}_z^{(n)}(r, \phi) \exp(i\omega t) \mathbf{e}_z \right), \quad (4)$$

$$\mathbf{E}^{(n)}(r, \phi, t) = \text{Re} \left(\underline{E}_r^{(n)}(r, \phi) \exp(i\omega t) \mathbf{e}_r + \underline{E}_\phi^{(n)}(r, \phi) \exp(i\omega t) \mathbf{e}_\phi \right). \quad (5)$$

In plasma, additionally, the charge density ρ and the current density \mathbf{j} are considered:

$$\rho(r, \phi, t) = \text{Re} \left(\underline{\rho}(r, \phi) \exp(i\omega t) \right), \quad (6)$$

$$\mathbf{j}(r, \phi, t) = \text{Re} \left(\underline{j}_r(r, \phi, t) \exp(i\omega t) \mathbf{e}_r + \underline{j}_\phi(r, \phi) \exp(i\omega t) \mathbf{e}_\phi \right). \quad (7)$$

The fields obey the full set of Maxwell equations, with electrical specifications for each zone. In the plasma, the equations are:

$$\frac{1}{\mu_0} \frac{1}{r} \frac{\partial \underline{B}_z^{(p)}}{\partial \phi} = \underline{j}_r + \varepsilon_0 i\omega \underline{E}_r^{(p)}, \quad (8)$$

$$-\frac{1}{\mu_0} \frac{\partial \underline{B}_z^{(p)}}{\partial r} = \underline{j}_\phi + \varepsilon_0 i\omega \underline{E}_\phi^{(p)}, \quad (9)$$

$$\frac{1}{r} \frac{\partial (r \underline{E}_\phi^{(p)})}{\partial r} - \frac{1}{r} \frac{\partial \underline{E}_r^{(p)}}{\partial \phi} = -i\omega \underline{B}_z^{(p)}. \quad (10)$$

The cold plasma model is invoked which contains the equation of continuity

$$i\omega \underline{\rho} + \frac{1}{r} \frac{\partial (r \underline{j}_r)}{\partial r} + \frac{1}{r} \frac{\partial \underline{j}_\phi}{\partial \phi} = 0, \quad (11)$$

and the equation of motion, where ω_{pe} is the plasma frequency and ν the collision rate

$$i\omega \underline{j}_r = \varepsilon_0 \omega_{pe}^2 \underline{E}_r - \nu \underline{j}_r, \quad (12)$$

$$i\omega \underline{j}_\phi = \varepsilon_0 \omega_{pe}^2 \underline{E}_\phi - \nu \underline{j}_\phi. \quad (13)$$

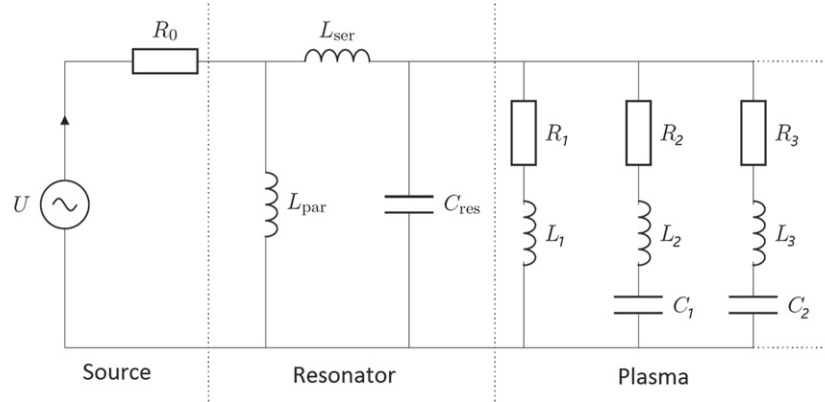


Figure 3. Lumped element representation of the double jet, consisting of the power source with $Z_0 = 50\Omega$, the resonator and the plasma itself. The matching network is included in the resonator. The capacitive coupling is taken into account as an infinite number of LCR-circuits (for $m = 1, 2, \dots$ while the inductive coupling is represented as an RL-circuit ($m = 0$)).

With the help of the relative plasma permittivity

$$\varepsilon_p = 1 - \frac{\omega_{pe}^2}{\omega^2 - i\omega\nu}, \quad (14)$$

the electric field can be expressed as

$$\underline{E}_r^{(p)} = \frac{c^2}{i\omega\varepsilon_p} \frac{1}{r} \frac{\partial \underline{B}_z^{(p)}}{\partial \phi}, \quad (15)$$

$$\underline{E}_\phi^{(p)} = -\frac{c^2}{i\omega\varepsilon_p} \frac{\partial \underline{B}_z^{(p)}}{\partial r}. \quad (16)$$

A second order differential equation for the magnetic field arises:

$$-\frac{1}{r} \frac{\partial}{\partial r} r \frac{\partial \underline{B}_z^{(p)}}{\partial r} - \frac{1}{r^2} \frac{\partial^2 \underline{B}_z^{(p)}}{\partial \phi^2} = \frac{\omega^2}{c^2} \varepsilon_p \underline{B}_z^{(p)}. \quad (17)$$

Within the plasma sheath, the Maxwell equations take the form:

$$\frac{1}{\mu_0} \frac{1}{r} \frac{\partial \underline{B}_z^{(s)}}{\partial \phi} = i\omega \underline{E}_r^{(s)}, \quad (18)$$

$$-\frac{1}{\mu_0} \frac{\partial \underline{B}_z^{(s)}}{\partial r} = \varepsilon_0 i\omega \underline{E}_\phi^{(s)}, \quad (19)$$

$$\frac{1}{r} \frac{\partial (r \underline{E}_\phi^{(s)})}{\partial r} - \frac{1}{r} \frac{\partial \underline{E}_r^{(s)}}{\partial \phi} = -i\omega \underline{B}_z^{(s)}, \quad (20)$$

which leads to

$$\underline{E}_r^{(s)} = \frac{c^2}{ri\omega} \frac{\partial \underline{B}_z^{(s)}}{\partial \phi}, \quad (21)$$

$$\underline{E}_\phi^{(s)} = -\frac{c^2}{i\omega} \frac{\partial \underline{B}_z^{(s)}}{\partial r}, \quad (22)$$

and

$$-\frac{1}{r} \frac{\partial}{\partial r} r \frac{\partial \underline{B}_z^{(s)}}{\partial r} - \frac{1}{r^2} \frac{\partial^2 \underline{B}_z^{(s)}}{\partial \phi^2} = \frac{\omega^2}{c^2} \underline{B}_z^{(s)}. \quad (23)$$

Within the dielectric, the equations are as follows, with permittivity $\varepsilon = \varepsilon_0 \varepsilon_r$:

$$\frac{1}{\mu_0} \frac{1}{r} \frac{\partial \underline{B}_z^{(d)}}{\partial \phi} = i\omega \varepsilon_0 \varepsilon_r \underline{E}_r^{(d)}, \quad (24)$$

$$-\frac{1}{\mu_0} \frac{\partial \underline{B}_z^{(d)}}{\partial r} = \varepsilon_0 \varepsilon_r i\omega \underline{E}_\phi^{(d)}, \quad (25)$$

$$\frac{1}{r} \frac{\partial (r \underline{E}_\phi^{(d)})}{\partial r} - \frac{1}{r} \frac{\partial \underline{E}_r^{(d)}}{\partial \phi} = -i\omega \underline{B}_z^{(d)}. \quad (26)$$

The electric field can be expressed as

$$\underline{E}_r^{(d)} = \frac{c^2}{i\omega \varepsilon_r} \frac{1}{r} \frac{\partial \underline{B}_z^{(d)}}{\partial \phi}, \quad (27)$$

$$\underline{E}_\phi^{(d)} = -\frac{c^2}{i\omega \varepsilon_r} \frac{\partial \underline{B}_z^{(d)}}{\partial r}. \quad (28)$$

A second order differential equation for the magnetic field arises:

$$-\frac{1}{r} \frac{\partial}{\partial r} r \frac{\partial \underline{B}_z^{(d)}}{\partial r} - \frac{1}{r^2} \frac{\partial^2 \underline{B}_z^{(d)}}{\partial \phi^2} = \frac{\omega^2}{c^2} \varepsilon_r \underline{B}_z^{(d)}. \quad (29)$$

At the boundaries between the zones, the fields have to fulfill certain continuity relations for the tangential components. Between plasma and sheath, they are

$$\underline{E}_\phi^{(p)}(R - d - \delta, \phi) = \underline{E}_\phi^{(s)}(R - d - \delta, \phi), \quad (30)$$

$$\underline{B}_z^{(p)}(R - d - \delta, \phi) = \underline{B}_z^{(s)}(R - d - \delta, \phi), \quad (31)$$

and between sheath and dielectric,

$$\underline{E}_\phi^{(s)}(R - d, \phi) = \underline{E}_\phi^{(d)}(R - d, \phi), \quad (32)$$

$$\underline{B}_z^{(s)}(R - d, \phi) = \underline{B}_z^{(d)}(R - d, \phi). \quad (33)$$

At $r = R$, the tangential field $\underline{E}_\phi^{(d)}$ vanishes, as long it is adjacent to the resonator walls. For $|\phi| < \arctan(d_s/2R) \approx d_s/2R$, however, it is equal to the constant capacitor field u/d_s , where u is the voltage at the gap:

$$\underline{E}_\phi^{(d)}(R, \phi) = \begin{cases} 0 & \text{for } |\phi| \geq d_s/2R \\ u/d_s & \text{for } |\phi| < d_s/2R. \end{cases} \quad (34)$$

Considering the specular symmetry of the configuration, the field equations can be solved by expansion into Fourier cosine

series. The solutions are as follows, where the J_m and the Y_m are Bessel functions of the first and second kind to order m , respectively:

$$\underline{B}_z^{(p)}(r, \phi) = u \sum_{m=0}^{\infty} C_m^{(p)} J_m \left(\sqrt{\varepsilon_p} \frac{\omega}{c} r \right) \cos(m\phi), \quad (35)$$

$$\underline{B}_z^{(s)}(r, \phi) = u \sum_{m=0}^{\infty} \left(C_m^{(s)} J_m \left(\frac{\omega}{c} r \right) + D_m^{(s)} Y_m \left(\frac{\omega}{c} r \right) \right) \cos(m\phi), \quad (36)$$

$$\underline{B}_z^{(d)}(r, \phi) = u \sum_{m=0}^{\infty} \left(C_m^{(d)} J_m \left(\sqrt{\varepsilon_r} \frac{\omega}{c} r \right) + D_m^{(d)} Y_m \left(\sqrt{\varepsilon_r} \frac{\omega}{c} r \right) \right) \cos(m\phi). \quad (37)$$

The coefficients $C_m^{(p)}$, $C_m^{(s)}$, $D_m^{(s)}$, $C_m^{(d)}$, and $D_m^{(d)}$ are determined by the continuity conditions. This results in the following system of linear equations:

$$\begin{pmatrix} 0 \\ 0 \\ 0 \\ 0 \\ c_m \\ d_s \end{pmatrix} = \begin{pmatrix} -J_m(b_p) & J_m(a_s) & Y_m(a_s) & 0 & 0 \\ -J'_m(b_p) & J'_m(a_s) & Y'_m(a_s) & 0 & 0 \\ \sqrt{\varepsilon_p} & 0 & -J_m(b_s) & -Y_m(b_s) & J_m(a_d) & Y_m(a_d) \\ 0 & -J_m(b_s) & -Y_m(b_s) & J_m(a_d) & Y_m(a_d) \\ 0 & -J'_m(b_s) & -Y'_m(b_s) & \frac{J'_m(a_d)}{\sqrt{\varepsilon_r}} & \frac{Y'_m(a_d)}{\sqrt{\varepsilon_r}} \\ 0 & 0 & 0 & \frac{icJ'_m(b_d)}{\sqrt{\varepsilon_r}} & \frac{icY'_m(b_d)}{\sqrt{\varepsilon_r}} \end{pmatrix} \begin{pmatrix} C_m^{(p)} \\ C_m^{(s)} \\ D_m^{(s)} \\ C_m^{(d)} \\ D_m^{(d)} \end{pmatrix}, \quad (38)$$

where the constants in the Bessel functions are abbreviations,

$$b_p = \sqrt{\varepsilon_p} \frac{\omega}{c} (R - \delta - d), \quad (39)$$

$$a_s = \frac{\omega}{c} (R - \delta - d), \quad (40)$$

$$b_s = \frac{\omega}{c} (R - d), \quad (41)$$

$$a_d = \sqrt{\varepsilon_r} \frac{\omega}{c} (R - d), \quad (42)$$

$$b_d = \sqrt{\varepsilon_r} \frac{\omega}{c} R, \quad (43)$$

and the coefficient c_m results from the expansion of the periodic rectangle function

$$c_m = \begin{cases} 1 & \text{for } m = 0 \\ \frac{1}{2R} \sin\left(\frac{md_s}{2R}\right) & \text{for } m \geq 1 \end{cases}. \quad (44)$$

For every azimuthal mode index m , the system of linear equation (38) can easily be solved. The resulting expressions are rather unwieldy but can be represented in a qualitative way, namely as the lumped element circuit ‘plasma’ of figure 3. Its subject is the electric current \underline{I} which flows into the cavity from the top electrode of the capacitor slit—identical, of course, because of symmetry, to the current which flows out of the cavity onto the bottom electrode. Evaluating the discontinuity condition for the magnetic field $\underline{B}_z^{(d)}$ at the cavity boundary,

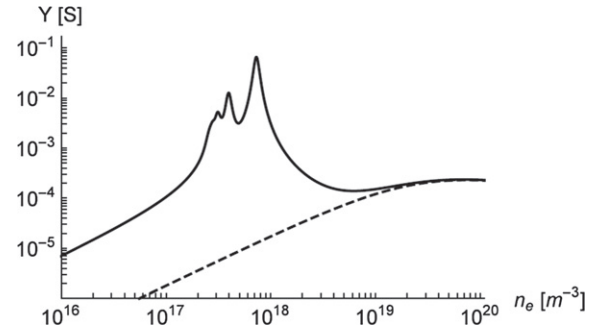


Figure 4. Real part of the complex admittance $Y(\omega, n_e)$ shown as a function of n_e for a constant frequency $\omega = 2\pi \times 2.45$ GHz. The dashed line represents the azimuthally symmetric mode $m = 0$, while the solid line represents the sum of all the modes.

one can deduce that

$$\underline{I} = \frac{L}{\mu_0} \underline{B}_z^{(d)}(R, 0) = u \frac{L}{\mu_0} \sum_{m=0}^{\infty} C_m^{(d)} J_m(b_d) + D_m^{(d)} Y_m(b_d). \quad (45)$$

This result suggests to represent the current I by an infinite number of parallel branches, each assigned to a mode m with an admittance

$$Y_m(\omega, n_e) = \frac{L}{\mu_0} (C_m^{(d)} J_m(b_d) + D_m^{(d)} Y_m(b_d)). \quad (46)$$

The mode $m = 0$ is non-resonant and behaves physically like an inductor–resistor circuit; the non-symmetric modes $m \geq 1$ are resonant and can be represented by LCR series circuits. (The identification is only qualitative, as the formulas involve transcendental functions and can only approximately be mapped to rational expressions.) Note that the ‘inductances’ in the circuits describe both magnetic and electron inertia effects. The total plasma admittance is shown in figure 4 and is the sum of the admittances of all branches,

$$Y_p = \sum_{m=0}^{\infty} Y_m(\omega, n_e), \quad (47)$$

and the current is

$$\underline{I} = \sum_{m=0}^{\infty} Y_m(\omega, n_e) u = Y_p(\omega, n_e) u. \quad (48)$$

The equivalent circuit can also represent the electromagnetic power P_{abs} that is fed to the jet. Applying Poynting’s theorem, integrating it over the cavity, and taking into account that the only non-metallic section of the boundary is the capacitor gap, we have

$$\frac{1}{2} P_{\text{abs}} = \frac{1}{4\mu_0} \int_G (\underline{\mathbf{E}} \times \underline{\mathbf{B}}^* + \underline{\mathbf{E}}^* \times \underline{\mathbf{B}}) \cdot d\mathbf{f} = Lu \frac{1}{2\mu_0} \text{Re}(B_z(R, 0)). \quad (49)$$

The factor 1/2 on the left reflects that the absorbed power P_{abs} is counted for the double jet, while $Y_p(\omega, n_e)$ was calculated for a single jet. Comparison shows that

$$\frac{1}{2} P_{\text{abs}}(\omega, n_e) = \frac{1}{2} \text{Re}(Y_p(\omega, n_e)) u^2. \quad (50)$$

As the impedance transformation network (see figure 3) is loss-less, the power absorbed in the MMWICP can also be expressed as with the source voltage of the power source u_s as

$$P_{\text{abs}}(\omega, n_e) = \frac{1}{2} \text{Re}(Y_s(\omega, n_e)) u_s^2, \quad (51)$$

Using the reflection coefficient defined above, the absorbed power can also be written as in terms of the incoming power P_0 :

$$P_{\text{abs}}(\omega, n_e) = (1 - |\Gamma(\omega, n_e)|^2) P_0 \quad (52)$$

4. Plasma model

This section enlists a so-called ‘global model’ to relate the discharge status in a single cavity to the absorbed electromagnetic power $P_{\text{abs}}/2$. Global models sacrifice spatial resolution [20]. Instead, they employ the volume-averaged balances of particle number and energy and amend them by some plausible *a priori* assumptions. Here, the effective discharge volume is defined as the geometric value $V_p = \pi(R - d)^2 L = 160 \text{mm}^3$; this reflects the assumption that the plasma column boundaries at $z = 0$ and $z = L$ are possibly blurred by edge effects but not drastically shifted. The volume-averaged particle balance is

$$\frac{dn_e}{dt} = K_{\text{iz}} n_g n_e - h \frac{A_m}{V_p} v_B n_e. \quad (53)$$

The first term on the right describes the particle gain via ionization from the ground state. (Stepwise ionization is neglected; it amounts to less than 20% of the ionization rate [21].) K_{iz} is the temperature-dependent ionization rate coefficient and $n_g = p/k_B T_g = 9.1 \times 10^{21} \text{m}^{-3}$ the argon neutral gas density. We adopt from [7] the form

$$K_{\text{iz}}(T_e) = 2.34 \times 10^{-14} (T_e/\text{eV})^{0.59} \exp(-17.44 \text{eV}/T_e) \text{m}^3/\text{s}. \quad (54)$$

The second term in (53) describes the loss of the plasma (=electron–ion pairs) to the column mantle of area $A_m = 2\pi(R - d)L = 125 \text{mm}^2$. We consider only losses in the radial direction; axial losses at $z = 0$ and $z = L$ are neglected. (There are no material boundaries there.) The Bohm speed is denoted by $v_B = \sqrt{T_e/m_i}$, with the ion mass of argon $m_i = 40 \text{AMU}$. The prefactor h , the so-called edge-to-center ratio [7], is calculated with the geometry data and an ion mean free path of $\lambda_i = 0.11 \text{mm}$:

$$h = 0.80(4 + (R - d)/\lambda_i)^{-1/2} = 0.15. \quad (55)$$

The second model equation describes the volume-averaged energy balance of the plasma. (Technically, the quantity considered as dynamic is the energy of the electron component; the energy of the ion component is algebraically related and thus not dynamic; see below.) The power P_{abs} coupled from the electromagnetic field to the electrons is balanced by the action of several power loss channels in the plasma and at the mantle. For a concise notation, we define the energy loss rate per electron as

$$R_\varepsilon(T_e) = K_{\text{iz}} n_g \varepsilon_{\text{iz}} + K_{\text{ex}} n_g \varepsilon_{\text{ex}} + K_{\text{el}} n_g \frac{3m_e}{m_n} T_e + h \frac{A_m}{V_p} v_B (2T_e + eV_{\text{sh}}). \quad (56)$$

The first term represents losses due to ionization, with the ionization energy $\varepsilon_{\text{iz}} = 15.76 \text{eV}$; the second term accounts for excitation, the excitation energy is $\varepsilon_{\text{ex}} = 12.14 \text{eV}$ and the corresponding rate coefficient is

$$K_{\text{ex}}(T_e) = 2.48 \times 10^{-14} (T_e/\text{eV})^{0.33} \exp(-12.78 \text{eV}/T_e) \text{m}^3/\text{s}. \quad (57)$$

The third term represents the energy loss via elastic collisions, the electron–neutral mass ratio is $m_e/m_n = 1.37 \times 10^{-5}$ and the rate coefficient is

$$K_{\text{el}}(T_e) = 2.336 \times 10^{-14} (T_e/\text{eV})^{1.609} \exp(0.0618 \ln^2(T_e/\text{eV}) - 0.1171 \ln^3(T_e/\text{eV})) \text{m}^3/\text{s}. \quad (58)$$

Finally, the kinetic energies carried off by the particles lost to the mantle are accounted for. For the electrons, assumed Maxwellian, the ratio of the energy flux to the particle flux is $2T_e$. Also, it is considered that the energy eV_{sh} gained by the ions in the sheath appears as a loss term in electron balance. A separate ion energy balance is not required; the transit time of the ion in the sheath is much shorter than the time constants considered in the global model. The sheath voltage, including the presheath contribution, is

$$V_{\text{sh}}(T_e) = \frac{T_e}{2e} \left(\ln \left(\frac{m_i}{2\pi m_e} \right) + 1 \right). \quad (59)$$

The volume-averaged energy balance can then be written as

$$\frac{d}{dt} \left(\frac{3}{2} n_e T_e \right) = \frac{P_{\text{abs}}}{2V_p} - R_\varepsilon n_e. \quad (60)$$

5. Characteristics of the system

Coupled together, the models of section 3 and 4 formulate a system of two nonlinear differential equations for the averaged plasma density n_e and the electron temperature T_e . With the dependence of the coefficients on the variables displayed explicitly, it reads:

$$\frac{dn_e}{dt} = K_{\text{iz}}(T_e) n_g n_e - h \frac{A_m}{V_p} \sqrt{\frac{T_e}{m_i}} n_e, \quad (61)$$

$$\frac{d}{dt} \left(\frac{3}{2} n_e T_e \right) = \frac{1}{2V_p} P_{\text{abs}}(\omega, n_e) - R_\varepsilon(T_e) n_e. \quad (62)$$

Of interest are the stationary solutions described by

$$K_{\text{iz}}(T_e) n_g n_e - h \frac{A_m}{V_p} \sqrt{\frac{T_e}{m_i}} n_e = 0, \quad (63)$$

$$\frac{1}{2V_p} P_{\text{abs}}(\omega, n_e) - R_\varepsilon(T_e) n_e = 0. \quad (64)$$

In equation (63), the plasma density cancels; a numerical root finding procedure gives an electron temperature of

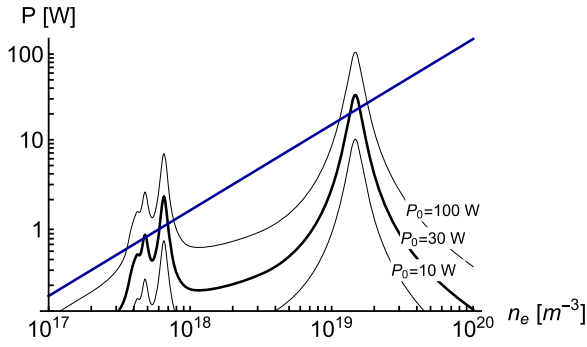


Figure 5. Absorbed power P_{abs} and loss power P_{loss} (blue line) for the double jet as functions of n_e . P_{abs} is shown for three different incident powers P_0 . The intersections of both curves represent stationary points of the model; they are stable (and thus possible operating points) when the P_{abs} -curve crosses from above.

$T_e = 2.46\text{eV}$. The energy loss rate per electron can then be found as $R_\epsilon = 2.95 \times 10^7 \text{eVs}^{-1}$, and the equilibrium condition for the jet model is thus

$$P_{\text{abs}}(\omega, n_e) = P_{\text{loss}}(n_e) \equiv 2R_\epsilon V_p n_e = 1.49 \times 10^{-18} \text{Wm}^3 n_e. \tag{65}$$

The structure of this equation invites a graphical interpretation. In figure 5 shows the absorbed power $P_{\text{abs}}(\omega, n_e)$ as a function of n_e for various values of the incident microwave power P_0 . The second curve is the straight line $P_{\text{loss}}(n_e) = 2R_\epsilon V_p n_e$.

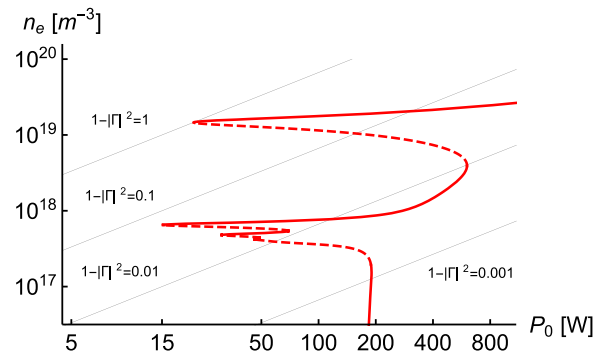


Figure 6. Stable (solid) and unstable (dashed) stationary points in the plane P_0 (incident power) and n_e (plasma density). $1 - |\Gamma|^2$ represents the fraction of P_0 that is absorbed by the plasma.

The intersections of the curves represent the stationary points of the model. When $P_{\text{abs}}(\omega, n_e)$ crosses $P_{\text{loss}}(n_e)$ from above, the stationary point (n_e, T_e) is stable and represents an operating point that can be realized. When $P_{\text{abs}}(\omega, n_e)$ crosses from below, the stationary point is unstable. This follows from the stability criterion discussed in the appendix,

$$\frac{\partial P_{\text{abs}}}{\partial n_e} < 2R_\epsilon V_p \Leftrightarrow \text{Operation point } (n_e, T_e) \text{ is stable.} \tag{66}$$

For a given incident power P_0 , the equilibrium condition can have more than one solution. Figure 6 shows the system

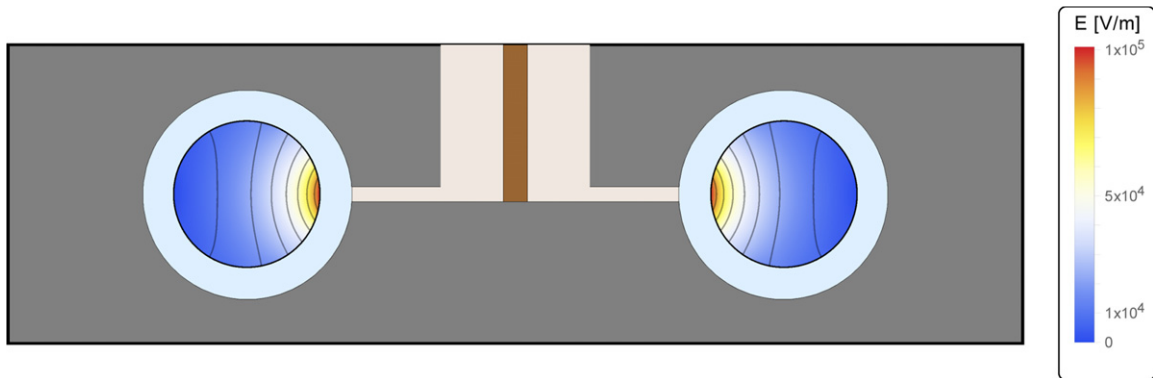


Figure 7. Electric field lines and field strength in the E -mode at $n_e \approx 6 \times 10^{17} \text{m}^{-3}$ and $P_{\text{abs}} = 10\text{W}$. The dielectric tube is shown in light blue.

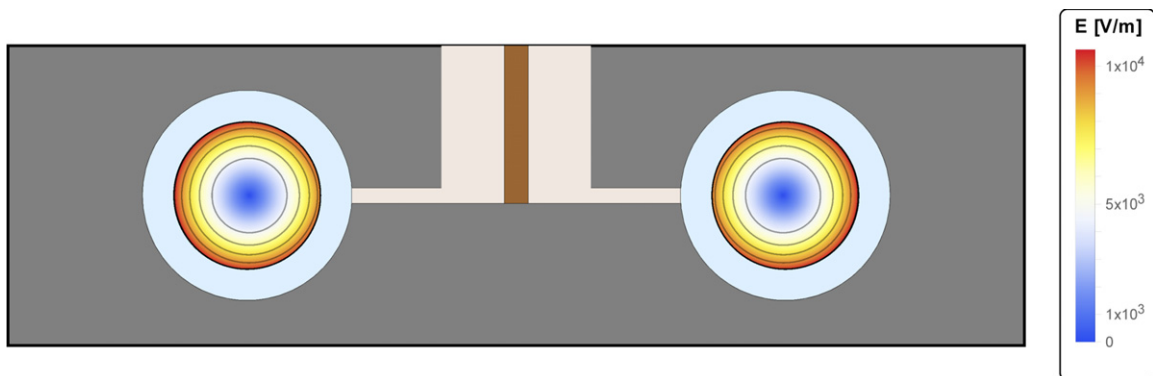


Figure 8. Electric field lines and field strength in the H -mode at $n_e \approx 10^{19} \text{m}^{-3}$ and $P_{\text{abs}} = 25\text{W}$. The dielectric tube is shown in light blue.

characteristics in the P_0 - n_e -plane. The stable stationary points are represented by the solid section, the unstable stationary points by the dashed section. The thin lines indicate value of the quantity $1 - |\Gamma(\omega, n_e)|^2$ which measures the fraction of the incoming power that is absorbed by the plasma.

Two separate regimes can be identified. They operate at comparable incident power levels, but are of physically different character. The first regime has a poor coupling efficiency, only 6% of the incident power is absorbed, and also a low plasma density of $n_e \approx 6 \times 10^{17} \text{m}^{-3}$. We identify this regime with the capacitive E -mode: the discharge current is carried by the asymmetric modes represented by the LCR series circuits, primarily by the mode $m = 1$. This interpretation is corroborated by the field line pattern shown in figure 7.

The second regime has a much better coupling efficiency. The electron density is a factor of 20 higher and exceeds $n_e = 10^{19} \text{m}^{-3}$. We identify this mode with the inductive H -mode, as the azimuthally symmetric mode $m = 0$ —which makes up to the non-resonant LR-branch of the lumped element equivalent circuit (see figure 4)—constitutes the dominant contribution. Again, this interpretation is supported by the plot of the electric field lines shown in figure 8. The field lines are nearly circular, and the influence of the skin effect is clearly visible.

From the solution diagram, we can infer that the MMWICP exhibits a pronounced hysteresis when cycling between the two discharge regimes. The behavior of the E to H transition can be observed also in other inductively coupled plasmas [22].

6. Summary and conclusion

In this work, the miniature microwave ICP (MMWICP), a microwave driven plasma jet based on the principle of inductive coupling, was investigated via mathematical modeling. An argon-fed double jet with a pressure of $p = 100 \text{Pa}$ and a gas temperature of $T_g = 800 \text{K}$ was taken as example. Two separate submodels were formulated. To describe the electromagnetic fields \mathbf{E} and \mathbf{B} , the full set of Maxwell's equations was analytically solved in the frequency domain by means of an infinite Fourier series. The solution was cast in the form of a lumped-element equivalent circuit which included also a model of the matching network. For the plasma itself, the volume-averaged balance equations for the particle number and the electron energy were formulated. The self-consistent coupling of the two submodels resulted in a system of two nonlinear differential equations for the volume-averaged plasma density n_e and the electron temperature T_e . The stationary points and their stability were analyzed. Two different operating regimes could be identified, the capacitive E -mode with a plasma density of $n_e \approx 5 \times 10^{17} \text{m}^{-3}$, and the inductive H -mode with densities of $n_e \geq 10^{19} \text{m}^{-3}$. The form of the E to H transition indicated a pronounced hysteresis behavior.

Our modeling results are in good qualitative agreement with the outcome of technological and experimental investigations conducted in parallel [18, 19]. This applies in particular to the existence of different discharge modes, their electron densities, and their symmetries. A more detailed comparison is, at

this point, not feasible: owing to its drastic simplifications, the global model presented in this work claim only qualitative, not quantitative validity. Moreover, the process gas here was argon, while the experiments were conducted in nitrogen. Future investigations to correct this deficiencies are already underway.

Acknowledgments

The authors gratefully acknowledge support by Deutsche Forschungsgemeinschaft DFG via the project 389090373.

Appendix A

This appendix contains a stability analysis of the stationary points of the MMWICP model. We linearize the dynamic equations (53) and (60) around the solutions of (63) and (64) with the following approach for the electron density and electron temperature

$$n_e(t) \rightarrow n_e (1 + \delta n_e(t)), \quad (\text{A1})$$

$$T_e(t) \rightarrow T_e (1 + \delta T_e(t)). \quad (\text{A2})$$

Two coupled linear first order differential equations arise. With the following abbreviations, all evaluated at the stationary point under consideration,

$$a_{12} = -\frac{1}{2} h \frac{A_m}{V_p} v_B + \frac{\partial K_{iz}}{\partial T_e} n_g T_e, \quad (\text{A3})$$

$$a_{21} = \frac{2}{3 T_e} \left(\frac{1}{2 V_p} \frac{\partial P_{\text{abs}}}{\partial n_e} - R_\epsilon \right), \quad (\text{A4})$$

$$a_{22} = -2 \frac{m_e}{m_n} \frac{\partial}{\partial T_e} (K_{el} T_e) n_g - \frac{\partial K_{iz}}{\partial T_e} n_g \left(\frac{2}{3} \epsilon_{iz} + T_e \right) - \frac{2}{3} \frac{\partial K_{ex}}{\partial T_e} n_g \epsilon_{ex} - h v_B \frac{A_m}{V_p} \left(2 + \frac{1}{2} \ln \left(\frac{m_i}{2 \pi m_e} \right) \right), \quad (\text{A5})$$

we can cast the dynamic equation as

$$\frac{d}{dt} \begin{pmatrix} \delta n_e \\ \delta T_e \end{pmatrix} = \begin{pmatrix} 0 & a_{12} \\ a_{21} & a_{22} \end{pmatrix} \begin{pmatrix} \delta n_e \\ \delta T_e \end{pmatrix}. \quad (\text{A6})$$

The character of the linearized model and the stability of the stationary point depends on the eigenvalues λ of the matrix A . If both eigenvalues are negative, the linearized solutions decay and the stationary point is stable. If one of them is positive, the linearized solutions grow and the stationary point is unstable. Explicitly, the eigenvalues read





$$\lambda_{1,2} = \frac{1}{2} a_{22} \pm \sqrt{a_{12} a_{21} + \frac{1}{4} a_{22}^2}. \quad (\text{A7})$$

Evidently, the coefficient a_{22} is always negative. Both eigenvalues are thus negative when the square root term is smaller than $|a_{22}|$, i.e., when $a_{12} a_{21}$ is negative. As a_{12} is always positive, the decision depends on the sign of a_{21} . This shows the

validity of the criterion used above: the stationary points of the jet model are stable under the condition

$$\frac{\partial P_{\text{abs}}}{\partial n_e} < 2V_p R \epsilon. \quad (\text{A8})$$

ORCID iDs

Michael Klute  <https://orcid.org/0000-0002-8062-896X>
 Horia-Eugen Porteanu  <https://orcid.org/0000-0001-9472-1041>
 Ilija Stefanović  <https://orcid.org/0000-0002-1652-1287>
 Ralf Peter Brinkmann  <https://orcid.org/0000-0002-2581-9894>

References

- [1] Lucovsky G and Tsu D V 1987 *J. Non-Cryst. Solids* **97–98** 265
- [2] Schütze A, Jeong J Y, Babayan S E, Park J, Selwyn G S and Hicks R F 1998 *IEEE Trans. Plasma Sci.* **26** 1685
- [3] Tendero C, Tixier C, Tristant P, Desmaison J and Leprince P 2006 *Spectrochim. Acta Part B* **61** 2
- [4] Laroussi M and Akan T 2007 *Plas. Process. Polym.* **4** 777
- [5] Kong M G, Ganguly B N and Hicks R F 2012 *Plasma Sources Sci. Technol.* **21** 030201
- [6] Winter J, Brandenburg R and Weltmann K-D 2015 *Plasma Sources Sci. Technol.* **24** 064001
- [7] Lieberman M A and Lichtenberg A J 2005 *Principles of Plasma Discharges and Materials Processing* (New York: Wiley)
- [8] Hopwood J 1992 *Plasma Sources Sci. Technol.* **1** 109
- [9] Godyak V 2002 *IEEE Ind. Appl. Mag.* **8** 1077–2618
- [10] Halfmann H, Bibinov N, Wunderlich J and Awakowicz P 2007 *J. Phys. D: Appl. Phys.* **40** 4145
- [11] Okumura T 2010 *Phys. Res. Int.* **2010** 164249
- [12] Godyak V 2013 *J. Appl. Phys.* **46** 283001
- [13] Reed T 1961 *J. Appl. Phys.* **32** 821
- [14] Ichiki T, Koidesawa T and Horiike Y 2003 *Plasma Sources Sci. Technol.* **12** 16
- [15] Yin Y, Messier J and Hopwood J A 1999 *IEEE Trans. Plasma Sci.* **27** 1516
- [16] Hopwood J A 2000 *J. Microelectromech. Syst.* **9** 309
- [17] Porteanu H-E, Gesche R and Wandel K 2013 *Plasma Sources Sci. Technol.* **22** 035016
- [18] Stefanović I, Bibinov N, Porteanu H-E, Klute M, Brinkmann R P and Awakowicz P 2018 *Plasma Sources Sci. Technol.* **27** 12LT01
- [19] Porteanu H-E, Stefanović I, Bibinov N, Klute M, Awakowicz P, Brinkmann R P and Heinrich W 2019 *Plasma Sources Sci. Technol.* **28** 035013
- [20] D Monahan D and Turner M M 2017 *Plasma Sources Sci. Technol.* **18** 245203
- [21] Kemaneci E, Mitschker F, Rudolph M, Szeremley D and Eremin D 2017 *Plasma Sources Sci. Technol.* **50** 245203
- [22] Daltrini A M, Moshkalev S A, Morgan T J, Piejak R B and Graham W G 2008 *Appl. Phys. Lett.* **92** 061504